Applied Surface Science 743 (2026) 167107

Contents lists available at ScienceDirect

Applied Surface Science

journal homepage: www.elsevier.com/locate/apsusc

Full length article

Response of a quartz crystal microbalance to a localized heat source: The case of MeV ion irradiation

Martina Fellinger [a,*], Eduardo Pitthan [b], Christian Cupak [a], Friedrich Aumayr [a], Daniel Primetzhofer [b], Michael Schmid [c]

[a] Institute of Applied Physics, TU Wien, Fusion@ÖAW, Vienna, Austria
[b] Department of Physics and Astronomy, Uppsala University, Uppsala, Sweden
[c] Institute of Applied Physics, TU Wien, Vienna, Austria

ARTICLE INFO

Keywords:
Quartz crystal microbalance
Ion beam analysis
Thermal stress
Temperature effect
Radiation damage

ABSTRACT

Quartz crystal microbalances (QCMs) are capable of detecting mass changes down to 10 pg cm^{-2} s^{-1}, but thermal and stress effects must be accounted for, even when SC-cut (stress-compensated) crystals are used. In this study, we examine the compatibility of two measurement techniques: A high-sensitivity QCM and ion beam analysis (IBA). When used hand in hand, IBA can complement the information obtained from a QCM by providing element-specific data. Our results show that the QCM operation is strongly influenced by the power dissipation of the ion beam. Since QCM operation requires thermal equilibrium, IBA should be performed after the QCM measurements. Large frequency changes occur during irradiation and the thermal relaxation after irradiation. We model these effects, which are due to both the direct temperature effect on the frequency and the influence of thermal stress. The frequency response has a fast and a slow component. The fast frequency change (within ≈1 s) is related to the inhomogeneous temperature distribution in the quartz plate, while the slow component is due to the low thermal conductivity between the quartz crystal and the holder. Further effects such as the influence of the beam damage on the crystal frequency are discussed.

1. Introduction

A quartz crystal microbalance (QCM) is a versatile tool widely used to quantify mass changes, particularly in monitoring layer growth during thin film deposition [1–6]. It can also provide quantitative information on mass changes during sputtering, which is important for various applications. In nuclear fusion, for example, plasma-facing components in fusion reactors are bombarded by fuel or seeding gas ions, leading to surface erosion [7–9]. Recent studies have successfully used the QCM technique to quantify relevant erosion cases [10–13] as well as implantation [14]. Similarly, it is feasible to investigate the erosion of planetary bodies lacking a protective atmosphere through laboratory experiments that mimic space weathering effects [15–18]. For all these applications, QCMs stand out by their high sensitivity allowing detection of mass changes down to 10 pg cm^{-2} s^{-1} [10,19]. For gold, this corresponds to $\approx 2 \times 10^{-5}$ monolayers per second. However, QCMs can only detect net mass changes, but cannot provide information on mass change by individual elements, which is crucial when studying compound materials: Effects like preferential sputtering or simultaneous mass changes by implantation and sputtering cannot be disentangled using a QCM only. Therefore, complementary approaches that can close this gap are desired to gain further information during erosion experiments.

Standard IBA techniques are Rutherford backscattering spectrometry (RBS) [20] and elastic recoil detection analysis (ERDA) [21]. In both cases, an ion beam, typically in the MeV energy range, is directed onto a sample of interest and either backscattered projectiles (for RBS) or scattered recoils (for ERDA) are detected. While ERDA is an efficient tool for detecting light elements, RBS is most efficient in the quantification of heavy elements. A full IBA setup, combining both RBS and ERDA, thus provides a powerful elemental analysis tool for a wide range of applications [22]. However, IBA is usually blind to surface erosion, as long as the composition remains unchanged and the change of the film thickness is below the sensitivity limit. Combining a QCM sensor with IBA techniques is therefore highly desirable from two perspectives. IBA and QCM provide complementary information; the elemental composition is given by IBA and the erosion or deposition rate in terms of mass change is measured by the QCM. A combination of both experimental techniques could, in principle, enable new measurement procedures and broaden the scope for future erosion experiments.

* Corresponding author.
E-mail addresses: fellinger@iap.tuwien.ac.at (M. Fellinger), aumayr@iap.tuwien.ac.at (F. Aumayr).

https://doi.org/10.1016/j.apsusc.2026.167107
Received 24 January 2026; Received in revised form 17 April 2026; Accepted 1 May 2026
Available online 6 May 2026

First experiments using a combination of IBA and QCM have been presented in Ref. [23] and show a significant influence of the MeV ion beam on the crystal frequency. However, the reasons for this response of a QCM to MeV ion beams have not been investigated so far.

In typical applications as a deposition monitor, a QCM experiences thermal loads of several eV per deposited atom (latent heat upon condensation plus thermal radiation from the evaporation source). For sputtering measurements, the energy deposited is higher, usually in the order of 1 keV per sputtered atom [10,11]. In these applications, the energy deposited is typically spread out over a comparably large area on the quartz crystal. While standard (low-cost) AT-cut quartz crystals are usually sufficient for deposition monitoring, the higher thermal load and the associated thermal stress during sputtering experiments make it advisable to use the SC (stress-compensated) cut, since its frequency has a vanishing sensitivity to radial stress [24]. In an IBA setup, the energy per incident ion is much higher, typically in the low MeV range, and the beam is usually focused, exacerbating the problems of temperature increase and thermal stress. The main aim of this study is to investigate the influence of MeV ion irradiation on a highly sensitive QCM. Therefore, we tested the response of the QCM during several beam-on and beam-off phases, with different ion energies, currents, and positions of the ion beam on the quartz crystal. The MeV beam is a local heat source; the arising temperature distribution was modeled by finite-element method (FEM) analysis, and the distribution of thermal stress as well as the change of the resonance frequency due to these influences was calculated. These calculations allow us to rationalize the effects observed in the experiment.

2. Materials and methods

2.1. Quartz crystal microbalance technique

In this study, we employed an SC-cut quartz crystal, manufactured by LapTech Precision Inc. The quartz crystal, a circular disk of 14 mm diameter, 6 MHz resonance (thickness 0.3 mm) and slightly plano-convex shape for energy trapping [25], is coated with a chromium (Cr) buffer layer of sub-nm thickness and additional gold (Au) electrodes of <100 nm thickness on both sides for electrical contact (see Appendix A for the RBS analysis of the electrodes). The lowest-frequency thickness-shear oscillation mode (usually named the C mode) of the quartz resonator can then be piezoelectrically excited by applying an alternating current to the gold electrodes (Fig. 1). It should be noted that the thicknesses of the crystal and gold electrode as well as the vibration amplitudes are strongly exaggerated in Fig. 1a.

In a simple one-dimensional model (assuming an infinite plate instead of the planoconvex shape), the resonance frequency of the quartz crystal depends on the crystal's thickness d and the sound velocity v for the relevant vibration mode; the latter can be expressed as $\sqrt{c/\rho}$, where ρ is the density and c an elastic constant:

$$f = \frac{v}{2d} = \frac{Z}{2m_A}. \quad (1)$$

The expression using the acoustic impedance $Z = \sqrt{c\rho}$ does not explicitly include the thickness d but the mass per area m_A, which is proportional to the thickness. In a perturbation approach, the sensitivity of the resonance frequency to changes of Z (or the relevant elastic constant) scales with the square of the strain or stress caused by the oscillation [26]. Therefore, the sensitivity on Z is highest in the central plane and vanishes at the surface, which is a nodal plane for the stress and strain of the vibration.

For sufficiently thin films deposited on the crystal (in case of Au, up to a few hundred nanometers), mass changes affect the resonance frequency linearly, which is described by the Sauerbrey equation [1]:

$$\frac{\Delta f}{f_0} = -\frac{\Delta m_A}{m_A}. \quad (2)$$

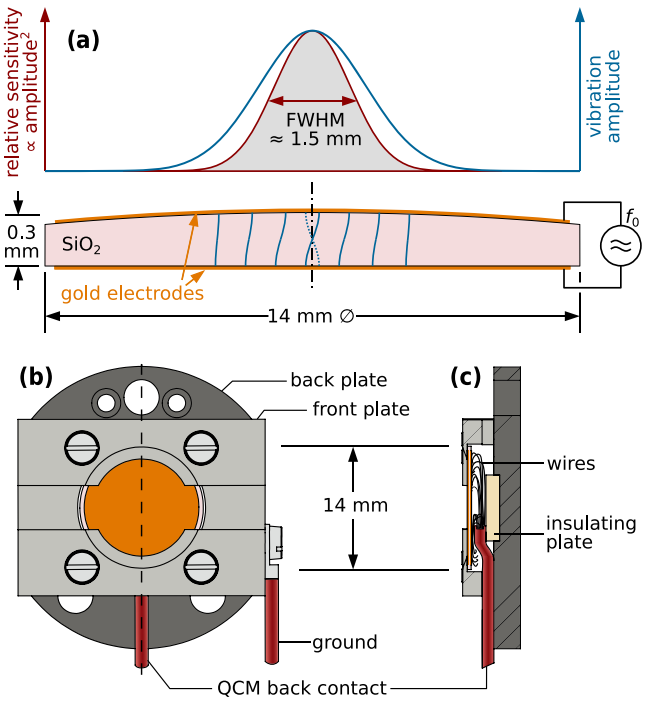

Fig. 1. (a) Schematic figure of the thickness-shear oscillation mode of the quartz crystal (not to scale), with the resonance frequency denoted as f_0. The sensitivity curve, which is proportional to the square of the oscillation amplitude, is shown at the top. (b) Sketch of the sample holder front view. (c) Cross-section of the sample holder along the dashed line marked in b.

Provided that the other physical variables affecting the resonance frequency remain constant, Eq. (2) provides a direct conversion of frequency changes Δf into changes of the mass per area Δm_A. Here, f_0 is the frequency before the mass change.

The plano-convex shape of the crystal leads to energy trapping. This means that the vibration amplitude is not constant over the full 14 mm-diameter area but close to a Gaussian distribution with the maximum at the center (where the local thickness of the plano-convex shape is highest) [25]. Again assuming first-order perturbation theory, the frequency change caused by any perturbation is proportional to the square of the amplitude (of acceleration for local mass changes, of strain or stress for changes of the elastic constants or acoustic impedance; all these follow the same Gaussian distribution as a function of the in-plane coordinates). For the crystal type used here, this Gaussian sensitivity function was determined to have a standard deviation of ≈0.76 mm (corresponding to a full width at half maximum FWHM of ≈1.5 mm) [17]. A visualization of the cross section of the quartz resonator, the thickness-shear oscillation together with the Gaussian sensitivity function is given in Fig. 1a.

The dependence of the resonance frequency on the temperature, $f(\vartheta)$, can be described by a third-order polynomial [27]. It should be noted that the exact temperature dependence can vary from crystal to crystal as it depends sensitively on the orientation of the crystal cut (mainly on the ψ angle, which mostly affects the linear term of the polynomial and thus also the temperatures of the minimum and maximum frequency [27]). As a consequence of the production process, the cut angle can be slightly different for different crystals. Two crystals from the same batch were used in the course of this study. The temperature dependence for one of the two crystals was measured and is shown in Fig. 2. The curve shows the resonance frequency of the crystal during a temperature ramp. The heating was realized in vacuum (≈10^{-8} mbar) by resistively heating the crystal holder and the corresponding temperature was logged via a thermocouple attached

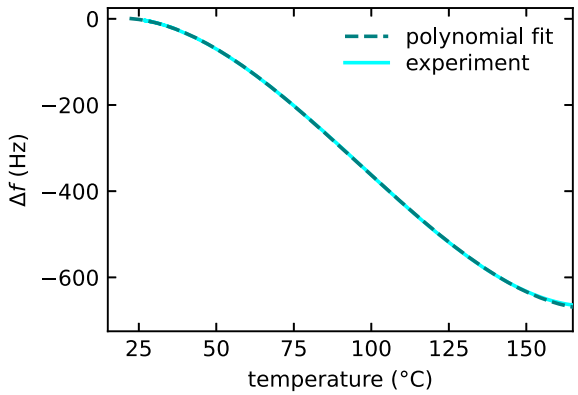

Fig. 2. Temperature dependence of the resonance frequency of a 6 MHz SC-cut quartz crystal. The vertical axis represents frequency differences $\Delta f = f - f_0$ with respect to the frequency f_0 at room temperature. The measured curve (cyan) was fitted by a third-order polynomial (dashed blue line), which is given in Eq. (3).

to the holder close to the quartz crystal. It should be noted that Fig. 2 presents data from a cool-down ramp conducted as part of a series of heating and cooling cycles intended to minimize the effect of potential outgassing during temperature increases. Superimposed on the experimental curve, also a third-order polynomial fit is shown:

$$\Delta f(\vartheta) = 3.69 \times 10^{-4}\,\vartheta^3 - 1.06 \times 10^{-1}\,\vartheta^2 + 3.62\,\vartheta - 31.3, \quad (3)$$

with the temperature ϑ in °C and the frequency change Δf in Hz. This will be used for further data analysis, described in Section 3.

In our setup, a dedicated electronic circuit is used to drive the crystal oscillation with a sinusoidal current. The phase of the electric impedance is used to detect any deviation from the resonance frequency and a control loop ensures that the resonance frequency is tracked [10, 19]. The frequency over time is recorded by a computer.

2.2. Ion beam analysis

We implemented the high-sensitivity QCM in an existing IBA setup located at the Tandem laboratory, Uppsala University, at the setup for in-situ growth, materials modification and analysis (SIGMA) [22,28]. The chamber is connected to a 5 MV Tandem accelerator and desired ion beams (masses ranging from ^{1}H to ^{197}Au and charge states up to 11+) can be directed into the chamber. In the course of this study, a He ion beam with ≈1 mm diameter and a top-hat profile was used. The beam was directed onto the quartz crystal at normal incidence. During experiments, the background pressure was in the order of 10^{-8} mbar within the chamber and the laboratory temperature was around 23.3 °C. Various IBA measurement approaches, including RBS and ERDA, can be conducted simultaneously, together with the QCM. The QCM is mounted via a crystal holder to a 6-axis goniometer, with a large thermal mass. The front view of the sample holder is sketched in Fig. 1b. A cut through the sample holder along the dashed line in Fig. 1b is shown in Fig. 1c, visualizing the contact on the back side of the QCM. The thermal conductance between the crystal and the crystal holder is expected to be low, as the contact surfaces are hard and rough, and only a few contact points are expected. Thermal conduction of these point contacts is low since both sides (the stainless-steel holder and the crystal) have a low thermal conductivity of about 10 $\mathrm{Wm^{-1}K^{-1}}$. Neither the temperature of the QCM nor that of the goniometer was actively controlled during the measurements.

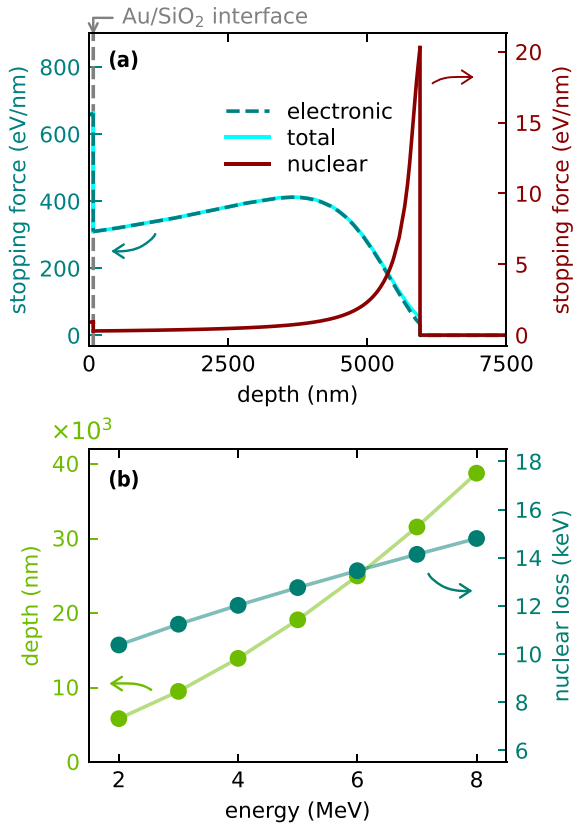

Fig. 3. SRIM [29] calculations for He impinging on a QCM target. (a) Projectile stopping force as a function of depth for 2 MeV He with normal incidence. The Au/SiO_2 interface is indicated by the dashed vertical line. The thickness of the Au electrode was determined by RBS (see Appendix A). (b) Depth at which the nuclear stopping force has its peak for different incident energies (left vertical axis, green) as well as the total nuclear loss as function of incident energy (right vertical axis, teal).

2.3. Simulation of ion transport and stopping

For a better understanding of the experiment, a simulation of the ion beam irradiation was performed. The SRIM software [29] was employed to study the interaction of MeV particles with a QCM sample. This software package can be used to generate tabulated electronic and nuclear stopping power values for different ion energies. These values were used to calculate the energy loss along the trajectory passing through the topmost Au electrode and the SiO_2 below. The results of this calculation for an initial energy of 2 MeV are shown in Fig. 3a. Additionally, the penetration depth (determined via the peak of nuclear stopping) of projectiles with different initial energies ranging from 2 MeV to 8 MeV is shown in Fig. 3b (left y-axis, light green). The nuclear energy loss, obtained by integrating the nuclear stopping force over depth, is shown in teal (right y-axis in Fig. 3b). The target layer structure of the simulation input, i.e. the thickness of the individual layers, was chosen according to IBA measurements (see Appendix A). The Cr buffer layer between Au electrode and SiO_2 disk was omitted due to its negligible contribution to the energy loss.

As seen in Fig. 3a, the impinging 2 MeV He ions are fully stopped at a depth of 5.9 µm; for 8 MeV they reach a depth of 38.8 µm (Fig. 3b). This is much less than the 300 µm thickness of the crystal. Additionally, it can be seen that despite the higher stopping power in the gold layer, the total energy loss within the gold electrode on the surface is negligible in comparison to the energy loss within the quartz crystal. We can therefore assume that the MeV particles are stopped only within the quartz and deposit almost all of their energy there. Fig. 3a

also visualizes that the energy is deposited mostly into the electronic system. Only a small fraction (<1%) of the total energy is deposited via nuclear collisions. The total nuclear loss depends only weakly on the energy (Fig. 3b), because it mainly occurs in the Bragg peak (close to the maximum depth), where the ion energy is low. The depth of this maximum of the nuclear stopping increases with increasing energy, meaning that the Bragg peak is located deeper in the sample for higher energies. The latter aspect is relevant for the influence of radiation damage discussed in Section 3.2.3.

2.4. FEM simulations

The temperature distribution and the thermal stresses in the quartz crystal were simulated using the open-source FEM program FreeFEM++ [30]. The geometry assumed was a spherical disk of 0.3 mm thickness, neglecting the radius-dependence of the thickness caused by the plano-convex shape. Since the disk is thin enough for the heat transport in thickness direction to be almost instantaneous, it is sufficient to solve a two-dimensional (2D) problem.

The relevant properties of quartz are anisotropic; thus, the respective tensors were rotated into the coordinate system of the SC-cut disk via a Mathematica script available in the supporting material, using the sign convention of the IEEE 1987 standard [31]. Since the SC-cut was historically derived from a rotated Y cut (the AT-cut, a disk with the normal direction obtained by rotating the y axis of the crystal structure of quartz [27]), the conventional coordinate system for AT- and SC-cut quartz crystals has the y axis in the thickness direction and the x and z axes in the plane. It should be noted that some material constants for a 2D calculation cannot be obtained by simply skipping the out-of-plane (y) components of the tensors; for the thermal conductivity λ and elasticity constants c one has to take the boundary conditions into account (see Appendix C). Notes on the implementation of the FEM calculations are given in Appendix D.

3. Results and discussion

3.1. Overview

An example frequency graph, monitored during a beam-on as well as the subsequent beam-off phase, is shown in Fig. 4. As the QCM technique is based on frequency changes, we plot Δf with respect to the frequency before switching on the beam at $t = 0$ s. Two separate exponential-decay fit functions for the beam-on (4 s < t < 906 s) and the beam-off phase (918 s < t < 1800 s) are shown as dashed lines in the plot. This experiment was conducted with a 2 MeV He^+ beam at normal incidence. The beam current of 9 nA corresponds to a power (thermal load on the crystal) of 18 mW.

Fig. 4 shows that two distinct effects in the QCM frequency appear as a result of switching the beam on and off. After switching on the beam at $t = 0$ s, a sharp peak is visible, occurring within a second or less. When the beam is switched off at $t = 900$ s, an inverse peak is observed; again instantaneous within the time resolution of the measurement. In the following, we will refer to these spikes as Δf^{on}_{fast} and Δf^{off}_{fast}, respectively. The second effect is a slow frequency drift over a time scale of hundreds of seconds, well described by the exponential fit mentioned above. In analogy to the instantaneous peaks, the sign of this drift is reversed after the beam is switched off. After ≈900 s after switching the beam on or off, the frequency comes close to an equilibrium value. The differences between the equilibrium value and the starting value will be called Δf^{on}_{slow} and Δf^{off}_{slow}.

To investigate these effects further, the beam energy E was varied between 2 MeV and 8 MeV and the beam current I was varied between 2 nA (singly charged He) and 18 nA (doubly charged He). This led to different powers $P = E \times I/q$ of the beam dissipated in the crystal, ranging from 6 mW to 72 mW. Here, q denotes the charge of the impinging ions. The resonance frequency curves for a large number of

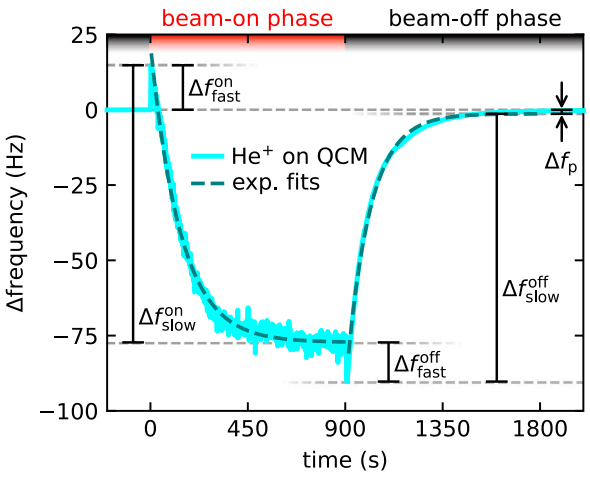

Fig. 4. Example frequency behavior during a beam-on and beam-off phase. The example shows the QCM resonance frequency during bombardment by a 2 MeV He^+ beam with a current of 9 nA (beam power 18 mW). The plot shows the frequency with respect to the initial value of ≈6 MHz. The beam was switched on at $t = 0$ s and switched off at $t = 900$ s.

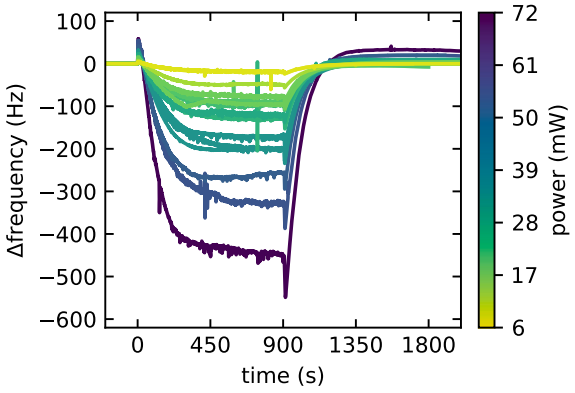

Fig. 5. Frequency behavior during a beam-on and beam-off phase for different beam power values. The power corresponding to each frequency graph is indicated by the color map. The absolute frequency values were shifted to zero before switching on the beam at $t = 0$ s. The beam was switched off at $t = 900$ s.

experiments are combined in Fig. 5. Each line represents a beam-on and a beam-off phase. The different colors correspond to beams with different impinging power.

Fig. 6 shows the fast (Δf^{on}_{fast}, Δf^{off}_{fast}) and the slow frequency changes (Δf^{on}_{slow}, Δf^{off}_{slow}) as a function of the beam power. It can be seen that both are roughly proportional to the power. It should be noted at this point that Figs. 5 and 6 show experimental data of various measurement runs conducted over several days. As discussed in Section 3.2.2, Δf_{fast} depends strongly on the exact position of the ion beam on the QCM. Therefore, we attribute some scatter of the Δf_{fast} values to small variations of the beam position.

Additionally, it is noticeable in Fig. 5 that the frequency curves do not always return to their initial values after the beam-on and subsequent beam-off period. These persistent frequency changes, further referred to as Δf_p (also marked in the example frequency graph in Fig. 4), are mostly positive and at least one order of magnitude smaller than the change Δf_{slow} during irradiation. These frequency differences between the final state after equilibration and the initial state are discussed in more detail in Section 3.2.3. Due to their relatively small magnitude, we neglected the influence of these persistent changes for most of our analysis.

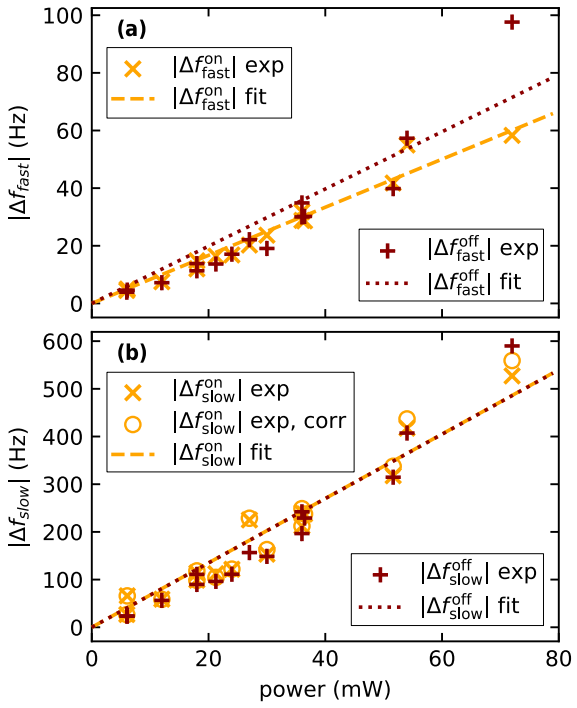

Fig. 6. Magnitude of the instantaneous frequency spike (a) and the slow frequency drift (b) as a function of the beam power. Besides the experimentally determined values, $\Delta f_{\text{fast}}^{\text{on}}$ exp, $\Delta f_{\text{fast}}^{\text{off}}$ exp and $\Delta f_{\text{slow}}^{\text{on}}$ exp, $\Delta f_{\text{slow}}^{\text{off}}$ exp, also linear fit functions are shown. The value "$\Delta f_{\text{slow}}^{\text{on}}$ exp, corr" was corrected by subtracting the persistent frequency change Δf_{p}, discussed in Section 3.2.3.

In summary, the frequency response caused by the MeV ion beam has three components, a fast one ($\lesssim$1 s) named Δf_{fast}, a slower exponential recovery Δf_{slow}, both reversible, and a persistent change Δf_{p}. The fast and slow changes scale approximately with the deposited power. For understanding these two time scales, we have to note that the thermal diffusivity of quartz is $\approx 4\,\text{mm}^2/\text{s}$. This means that vertical heat transport in the 0.3 mm thick quartz plate is essentially instantaneous and it takes less than one second to reach a local temperature equilibrium in the area heated by the ion beam (1 mm ⌀) and its immediate surroundings. Besides these first findings, further details on the three distinct effects Δf_{slow}, Δf_{fast} and Δf_{p} are discussed individually in the following Sections 3.2.1, 3.2.2, and 3.2.3, respectively.

3.2. Data analysis and simulations

3.2.1. The slow frequency drift Δf_{slow}

The slow frequency drift can be explained as a direct consequence of the beam-induced heating and the temperature dependence of the resonance frequency $\Delta f(\vartheta)$ (Fig. 2, Eq. (3)). We can use this $\Delta f(\vartheta)$ curve to calculate the temperature increase of the QCM from the frequency. The slow frequency drift occurs over a time frame much longer than required to obtain thermal equilibrium within the quartz plate. Thus, the slow temperature increase depends on the power impinging on the QCM (the beam power P), the heat capacity C of the crystal and the thermal resistance R_{th} between the crystal and its surroundings. Under these assumptions, in the most simple lumped-element thermal model, the crystal temperature during the beam-on phase starting at $t = 0$ s is given by

$$\vartheta(t) = \vartheta_0 + \Delta\vartheta\left(1 - e^{-t/\tau}\right), \text{ where} \tag{4}$$

$$\Delta\vartheta = R_{\text{th}}\,P, \text{ and} \tag{5}$$

$$\tau = R_{\text{th}}\,C\,. \tag{6}$$

Here, ϑ_0 is the ambient temperature, $\Delta\vartheta$ the temperature increase, and τ the time constant. Similarly, after switching off the beam at $t_1 = 900$ s, the temperature is given by

$$\vartheta(t) = \vartheta_0 + \Delta\vartheta\, e^{-(t-t_1)/\tau}, \tag{7}$$

with $\Delta\vartheta$ and τ again satisfying Eqs. (5) and (6), respectively.

Assuming linear $f(\vartheta)$ characteristics, these $\vartheta(t)$ functions would yield exponential relaxation curves for $f(t)$, which explains the good fit of the slow drift by exponential functions in Fig. 4. However, since the frequency is a nonlinear function of the temperature, for an exact determination of the crystal temperature, it is necessary to take the actual $f(\vartheta)$ curve into account (Fig. 2, Eq. (3)). This is especially true for the beam-off phase, where the temperature slowly approaches room temperature, which is close to the maximum of the $f(\vartheta)$ curve.

As argued later in Section 3.2.2, the instantaneous spike Δf_{fast} is not simply due to the $f(\vartheta)$ curve but mostly related to thermal stress. Thus, for simplicity, we take the frequency after this spike as the reference frequency $f(\vartheta_0)$ for the beam-on phase. For the beam-off phase we used the maximum frequency (around $t = 1800$ s) as reference frequency $f(\vartheta_0)$. The starting temperature ϑ_0, in our case room temperature, was set to 23.3 °C for all calculations, based on a laboratory temperature measurement.

Fig. 7 shows fits of the temperature $\vartheta(t)$ during (a) the beam-on and (b) the beam-off phases for different beam powers, where the temperature $\vartheta(t)$ was obtained by converting the frequency $f(t)$ into temperature $\vartheta(t)$ using the $f(\vartheta)$ curve. Since the heat capacity C of the crystal is known from its mass and the specific heat of quartz [32] [$C(\vartheta = 50\,°\text{C}) = 0.1004\,\text{g} \times 0.79\,\text{J/g}$], we can determine the thermal resistance R_{th} either from the time constant τ (Eq. (6)) or the temperature increase $\Delta\vartheta$ (Eq. (5)). The specific heat of quartz is actually temperature dependent; for simplicity, we used the value at an average temperature of $\vartheta = 50\,°\text{C}$. We also neglected the temperature dependence of the thermal conductivity, which decreases with temperature for quartz [33], but increases with temperature for stainless steel (the material of the crystal holder) [34].

We found an average time constant of $\tau \approx 134$ s, which translates into a thermal resistance of $R_{\text{th}} \approx 1688\,\text{K/W}$. With the other approach, from the $\Delta\vartheta$ values, Eq. (5) resulted in an average value of the thermal resistance of $R_{\text{th}} \approx 1717\,\text{K/W}$. The scatter of the individual R_{th} values is much larger than the difference between these two analysis methods, see Fig. 8. We attribute most of the scatter to the poorly defined point contacts between the quartz crystal and the stainless-steel holder; due to thermal expansion the contact points between the two rough surfaces may also change with temperature. The scatter of the time constants is also obvious when comparing the individual $f(t)$ or $\vartheta(t)$ curves (Figs. 5 and 7), especially for the curves in the beam-on phase. In addition to the random scatter, Fig. 8 also shows systematic effects: all thermal resistance values calculated from frequency measurements near room temperature (τ in the beam-off phase and $\Delta\vartheta$ for low beam power) are systematically at the high side. As the slope of the $f(\vartheta)$ curve is very low near room temperature, the conversion from frequency to temperature is inaccurate in this temperature range. An error of 5 K in the ambient temperature ϑ_0 or the temperature of the maximum of the $f(\vartheta)$ curve would have a ≈20% effect on these high R_{th} values, canceling much of the systematic trends mentioned and bringing the average R_{th} value down to 1625 K/W, calculated via Eq. (6), and 1536 K/W, calculated via Eq. (5).

In other words, any inaccuracies in the temperature measurement used for obtaining the $f(\vartheta)$ curve in Fig. 2 propagate to the calculation of the thermal resistance. One potential source of uncertainty arises from the fact that the temperature was measured via a thermocouple attached to the heated sample holder, but not to the quartz itself. Consequently, a discrepancy between the actual quartz crystal temperature and the measured value, cannot be ruled out. As mentioned, due to the small slope of the $f(\vartheta)$ curve near room temperature, inaccuracies in

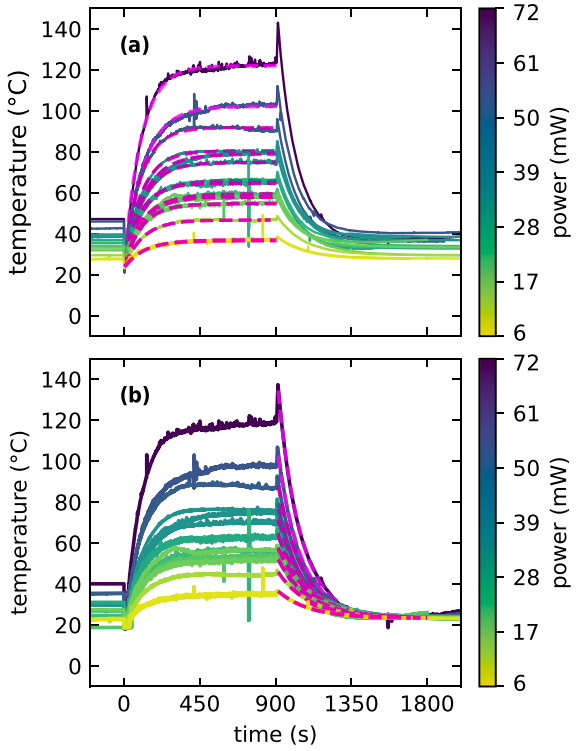

Fig. 7. Measured frequency curves $f(t)$ converted to temperature $\vartheta(t)$ (full curves) for different beam power values. The beam power in each case is indicated by the line color. The dashed lines (magenta) are exponential fits to $\vartheta(t)$ for (a) the beam-on phase and (b) the beam-off phase. For converting the frequency into temperatures, it was assumed for the beam-on phase that the negative Δf_{fast} peak immediately after switching the beam on corresponds to room temperature and the frequency change Δf was therefore set to $\Delta f = 0$ after the beam-on spike. For the beam-off phase, it was assumed that the maximal frequency within the beam-off phase (excluding outliers) corresponds to room temperature.

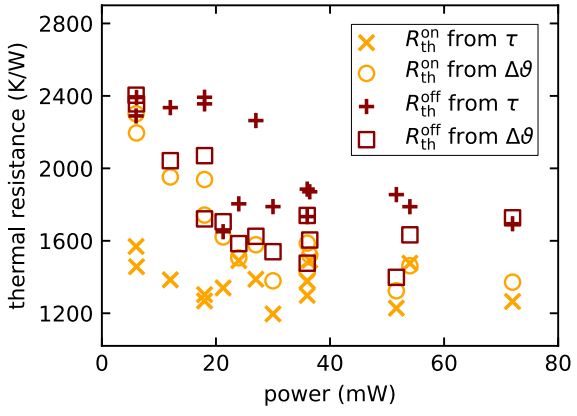

Fig. 8. Thermal resistance R_{th} as a function of applied power obtained from the fit functions. The R_{th} values are extracted from either the temperature change $\Delta\vartheta$ (Eq. (5)) or from the time constant τ (Eq. (6)).

this region have a comparably large influence on the calculated R_{th} values.

It should also be mentioned that the calculated values of R_{th} do not exactly correspond to the thermal resistance of the contact between the quartz crystal and the holder. On the one hand, part of the total thermal resistance is related to heat conduction between the near-center area of the crystal (where the beam impinges and the temperature is sensed,

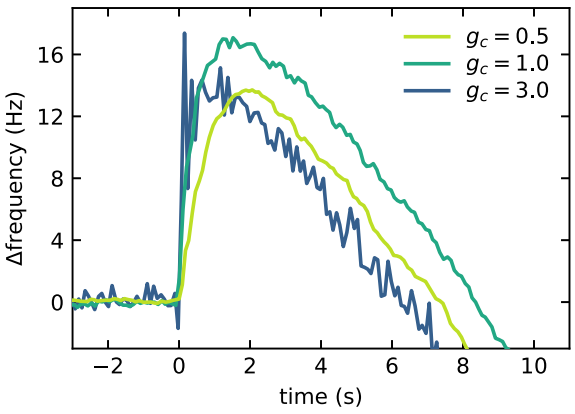

Fig. 9. Fast $\Delta f_{\text{fast}}^{\text{on}}$ spike measured with different gains g_c of the frequency control loop. The beam was switched on at $t = 0$ s. The beam power was 20 mW (2 MeV, 10 nA He^+). The different spike heights may be partly related to slightly different beam positions on the crystal or fluctuations in the beam current.

see Fig. 1) and its border. Based on our FEM simulations, which are discussed in more detail in the upcoming Section 3.2.2, this thermal resistance of the crystal corresponds to ≈100 K/W for beam incidence at the center, well below 10% of the total thermal resistance. On the other hand, some energy is transported by radiation. Assuming an emissivity of $\epsilon = 0.04$ for both, the upper and lower gold electrode of the crystal (which we consider an upper limit at the relevant wavelengths [35]), radiation alone would yield a value of $R_{\text{th}} \approx 13700$ K/W at room temperature. This is almost an order of magnitude higher than the experimental value of R_{th}. Thus, radiation contributes less than 15% to the heat transport from the quartz crystal to the surrounding.

We should finally mention that a temperature increase to more than 100 °C as found for the highest beam power in our study is not typical for IBA. In typical IBA experiments, the thermal conductivity between the sample and the holder is better. For a QCM, stress due to external forces can lead to frequency shifts, thus the crystal should be pressed against the holder with very gentle force, which leads to a high thermal resistance between the crystal and holder.

3.2.2. *The fast frequency spike* Δf_{fast}

As seen in Figs. 4 and 5, the beam-on spike $\Delta f_{\text{fast}}^{\text{on}}$ occurs quickly after the beam is switched on. With our electronics and data acquisition [10,19], we can modify the gain of the frequency-control loop; higher gains g_c lead to a faster response, but also increased noise and incipient instability (control loop oscillations) at very high g_c values. This can be clearly observed in Fig. 9. Nevertheless, the curve taken with the fastest setting ($g_c = 3$) indicates that the rise time of the fast spike is about 0.5–1 s.

The magnitude of the frequency spikes is proportional to the beam power (Fig. 6a), but strongly depends on the exact position where the beam impinges at the crystal surface. This can be seen in Fig. 10 (a) and (b), which shows $\Delta f(t)$ when switching the beam on for different impact positions, but constant beam power (20 mW). To consistently extract the spike sizes, we applied a linear fit to the decreasing trend within the time interval from $t = 3$ to $t = 5$ s. We then extrapolated this fit to $t = 0$ and read off the offset of the fit as a representative value for $\Delta f_{\text{fast}}^{\text{on}}$. An example fit is shown in Fig. 10a for measurement number 5.

The size and even the sign of the fast change varies largely between the measurements, it can be both positive and negative. A position map of these $\Delta f_{\text{fast}}^{\text{on}}$ values is shown in Fig. 10c. The sign and height of $\Delta f_{\text{fast}}^{\text{on}}$ for these incidence positions is visualized by the color, and the numbers refer to the curves in panels (a) and (b).

In the following, we will show that the main reason for this apparent spike is stress caused by thermal expansion. The beam power leads to

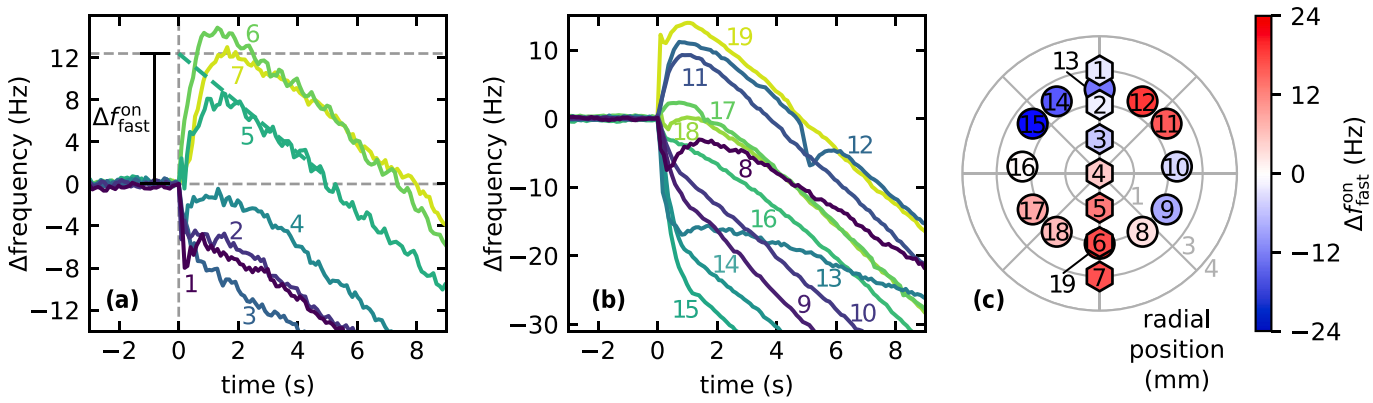

Fig. 10. Dependence of the fast frequency changes ("spikes") $\Delta f^{\mathrm{on}}_{\mathrm{fast}}$ on the position on the QCM. Panels (a) and (b) show the positive and negative spikes caused by switching on the beam at $t = 0$. The individual curves correspond to different positions on the QCM. The $\Delta f^{\mathrm{on}}_{\mathrm{fast}}$ values vs. beam position on the quartz crystal are shown by the colors in panel (c). Each marker is labeled with the curve number in panel (a) or (b). The beam power was 20 mW (2 MeV, 10 nA He^+).

a temperature increase at the impact position, which locally deforms the crystal. As mentioned above, the thermal diffusivity in quartz is $\approx 4\,\mathrm{mm}^2/\mathrm{s}$, which means that heat conduction in the vicinity of the impact area (1 mm ⌀) is fast. Therefore, the local stress field in the region relevant for the frequency change (Fig. 1) will quickly approach equilibrium. This stress is present as long as the beam remains on, and it is quickly released when the beam is switched off. Therefore, the fast change Δf_{fast} (the spike) is reversed when the beam is switched off. In other words, the stress effect on $\Delta f(t)$ is a (smoothed) step function at the switch-on time, and a reverse step when the beam is switched off. The slow changes Δf_{slow} are superimposed to this, which causes the appearance as a spike when the signs of Δf_{fast} and Δf_{slow} are opposite.

The response of a disk-shaped quartz crystal resonator to stress is well described in the literature for radial stress applied at two opposite points of the disk edge [36,37]. In this case, the frequency change is described by the force-frequency coefficient K_f, which depends on the azimuth angle ψ of the points where the stress is applied. For the C mode of SC-cut crystals, K_f is a roughly sinusoidal function of ψ. The average of $K_f(\psi)$ over the full azimuth range (0–180°) vanishes; hence the name "stress compensated".

For the case of a localized power source exactly at the crystal center, thermal expansion causes an almost isotropic compressive stress in the near-center region, as seen in the FEM simulations in Fig. 11. (Due to the anisotropy of the thermal conductivity and elastic constants, the two principal stresses at the center are not exactly identical; they differ by ≈8%.) Since the frequency of SC-cut crystals is insensitive to isotropic stress, the stress-induced frequency change is negligible for beam impact at the center. For off-center beams, the stress-sensitive area in the crystal center lies in a region of anisotropic stress, which can lead to a sizable frequency shift. The simulation yields stress-induced frequency changes of up to ±23 Hz for 20 mW beam power; the strongest effect occurs at beam positions 2.4 mm off center (Fig. 11c). The magnitude of the maximum stress-induced Δf in the simulations agrees very well with the maximum Δf_{fast} values in the experiment (Fig. 10c).

The center point in Fig. 10c shows a spike size of $\Delta f^{\mathrm{on}}_{\mathrm{fast}} \approx 5$ Hz (point 4 in Fig. 10), while the FEM calculation yields a vanishing effect of the thermal stress on the frequency at the center position. This discrepancy is likely due to a small error of the beam coordinates; the coordinate origin of Fig. 10c might not exactly coincide with the center of the crystal. The FEM calculations show that small deviations in the beam position will lead to comparably large errors regarding the stress effects due to the high sensitivity on the impact position: deviations by 0.6 mm can lead to errors in the order of 5 Hz.

The stress-induced frequency shift is not the only contribution to the fast response Δf_{fast}. In addition, also the temperature at the position of the impinging beam has a fast component not captured by the simple lumped-element model discussed in Section 3.2.1. Our FEM calculations for 20 mW beam power show that this fast component of the temperature, weighted with the Gaussian sensitivity curve of Fig. 1, amounts to 1.9 K for a beam position at the center and 0.6 K for a beam at $(x, y) = (1.5, 1.5)$ mm. Since the temperature during the measurement runs in Fig. 10 was not controlled and the experiments were taken in rapid succession without awaiting equilibrium, the exact slope of the $\Delta f(\vartheta)$ curve at $t = 0$ is only approximately known. Due to the short irradiation time compared to the idle time, the average power was low; therefore the initial temperature at each run was close to room temperature. Due to the flat slope of the $\Delta f(\vartheta)$ curve near room temperature, the influence of the temperature on the frequency was relatively small, weaker than $\mathrm{d}f/\mathrm{d}\vartheta = -1$ Hz/K. This implies that the effect of the fast component of the temperature is negligible compared to the observed $\Delta f^{\mathrm{on}}_{\mathrm{fast}}$ values in the range of ±24 Hz.

We should finally note that the compressive stress in the center of the crystal may also lead to bending. Due to the high power density per area of the beam ($25\,\mathrm{kW/m}^2$ at 20 mW beam power), the temperature difference between the front and back side of the crystal is on the order of 0.1 K in the irradiated area. The differences of thermal expansion on the front and back side of the crystal will lead to bending. For an MeV beam with a substantially higher beam power (up to 450 mW), Minagawa et al. [38] have observed a fast, reversible bending of a thin Si membrane (8 µm thick) by ≈95 µm. This bending is caused by the temperature gradient in the thickness direction and the radial compressive stress (with the latter being the dominant contribution). The quartz crystal is much thicker (0.3 mm) than this Si membrane, and therefore much stiffer. Therefore, bending of the crystal will be much less. Since the "neutral plane" of a bending deformation is the central plane, the effect of the positive and negative stress contributions of the bending deformation on the frequency will cancel out.

3.2.3. *Persistent frequency changes* Δf_p

As briefly mentioned in Section 3.1, ion beam irradiation causes a frequency change that remains after thermal equilibration. Fig. 12 shows this net frequency change induced by the ion bombardment for the data set of Fig. 5. This plot contains three sequences of consecutive irradiation experiments. Within one sequence, no idle time occurred between the beam-on/beam-off cycles. The first two sequences were obtained on a single day with few hours idle time in between, the third sequence was obtained on a different day. Except for one outlier, the persistent frequency change induced by the irradiation was positive. Even considering the different beam powers, it seems that the first experiment on a given day leads to a larger frequency change than experiments performed later on the same day. Since the persistent frequency change is usually positive, this allows us to rule out one very trivial explanation, a temperature increase of the crystal

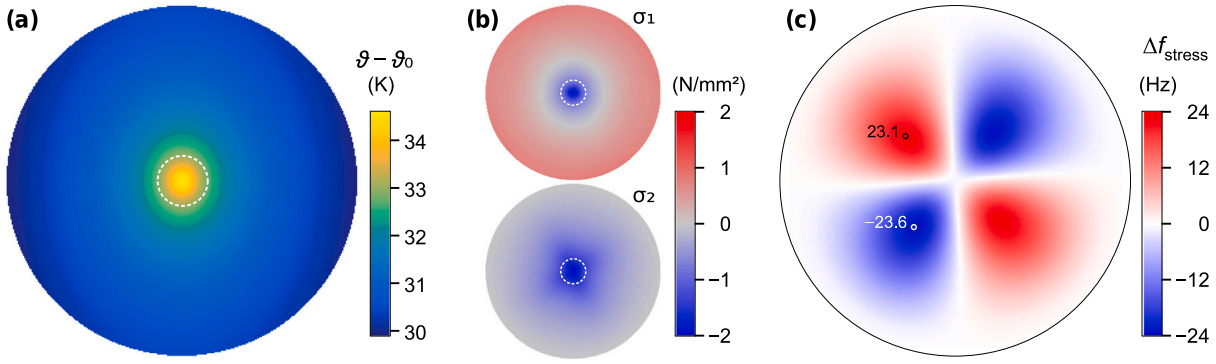

Fig. 11. Results of the FEM simulations for 20 mW beam power dissipated in a circular area of 1 mm diameter, shown as a dashed white circle in (a) and (b), where the beam position is at the center. The thermal resistance at the boundary was set to 1500 K/W. (a) Temperature distribution. (b) Principal stresses σ_1 and σ_2; except for the very center these roughly correspond to the tangential and radial stress, respectively. (c) Stress-induced frequency change vs. position of the beam center. The x direction of the crystal's coordinate system is to the right in all images, and the circular outlines are at the edge of the crystal (14 mm ⌀).

holder due to energy deposited on the quartz crystal. The $f(\vartheta)$ curve (Fig. 2) has its maximum slightly below room temperature; a temperature increase would cause a decrease, not an increase of the frequency. Several possible causes for frequency changes are remaining: (i) mass loss due to sputtering and/or thermal desorption, (ii) accumulation of electric charge in the bulk and (iii) radiation damage in the bulk of the crystal. These topics will be discussed individually in the following paragraphs.

(i) A positive frequency shift can correspond to a mass loss, caused by thermal desorption or sputtering. Based on Fig. 3, nuclear stopping near the surface is negligible, so we can exclude nuclear sputtering. Sputtering due to electronic transitions is not expected for the electrode material Au, but might occur for weakly bound adsorbates. The temperature increase may also lead to thermal desorption of weakly bound species. The temperature increases linearly with the beam power; but the desorption increases nonlinearly with temperature. Assuming thermal desorption from both sides of the crystal, the maximum frequency change of about 30 Hz in a single 900 s irradiation experiment corresponds to a loss of about 10 monolayers of H_2O per side or 2 monolayers of octanol (an arbitrary example of an organic molecule that might be weakly adsorbed). We consider these high adsorbate coverages very unlikely. For explaining the sum of the frequency shifts in the 3rd series of experiments of Fig. 12, one would have to hypothesize that even twice that coverage must be present or that adsorption in the beam-off phase replenishes the adsorbate coverage. The latter assumption is incompatible with the residual-gas pressure of 10^{-8} mbar in the chamber. Assuming sputtering, the mass loss per area in the irradiated region (1 mm ⌀) has to be about 10 times higher than in the thermal desorption scenario, since only part of the vibrating area of the quartz crystal and only the front side is affected by sputtering. Thus, neither thermal desorption nor sputtering can explain all of the persistent frequency change. Nevertheless, we consider it likely that thermal desorption is a contribution to the persistent frequency increase, especially for the first irradiation in each series of Fig. 12, where a substantial adsorbate coverage may have been present after exposure to the residual gas.

(ii) It has also been proposed that radiation-induced frequency changes could be due to high electric fields, caused by charges trapped in SiO_2 [39]. Assuming the voltage sensitivity of SC-cut resonators of 7×10^{-9} V^{-1} from Ref. [40], the highest frequency shift observed by us (≈30 Hz) would correspond to a voltage of ≈700 V in a one-dimensional model. In reality, the 1 mm-diameter beam (where charge is implanted) is smaller than the sensitive area of the crystal, which means that the voltage required for this frequency change would be five times larger. Assessing the actual charging of the quartz layer during irradiation is not straightforward, since the irradiation constantly induces conductive channels within the material. It is therefore expected that trapped charges can escape to the electrodes. Charging can only occur within the penetration depth of the ions, i.e. in the upper ≈38.8 μm for 8 MeV He. The electric field affects the resonance frequency via the acoustic impedance; as mentioned in Section 2.1, such an effect vanishes near the surface and only the field between the trapped charges and the back electrode will be relevant. This means that a frequency shift by ≈30 Hz requires a potential of ≈3000 V at a distance of 38.8 μm from the front electrode. This corresponds to a field of 80 MV/m, more than 10% of the breakdown field of unperturbed SiO_2 [41]. Considering the damage induced by the ions, we consider such a high field unrealistic. Additionally, the charge would build up in less than a second, thus an effect of the electric field would add to the fast frequency change $\Delta f^{\mathrm{on}}_{\mathrm{fast}}$, but not to $\Delta f^{\mathrm{off}}_{\mathrm{fast}}$. The equal magnitude of $\Delta f^{\mathrm{on}}_{\mathrm{fast}}$ and $\Delta f^{\mathrm{off}}_{\mathrm{fast}}$ seen in most data points of Fig. 6a rules out such an explanation for the persistent frequency changes. Furthermore, as the equilibrium charge would be obtained in less than a second, charging can only explain the persistent frequency change in the first experiment of a day (assuming that the charge implanted in previous days has disappeared), not the frequency changes in successive experiments as seen in the 3rd run of Fig. 12.

(iii) The effects of radiation damage on the resonance frequency of quartz crystals are hard to predict. Gamma radiation (which causes electronic excitations) may induce a frequency increase or decrease, even for SC-cut crystals that are largely insensitive to stress, and even for a single unit, depending on the radiation dose [42]. For high doses and irradiation by protons or neutrons (causing collisional damage), the usual effect is a frequency increase [43,44].

Based on the irradiation experiment by neutrons in Ref. [44], one can estimate a relative change of the frequency or acoustic impedance $\Delta f/f = \Delta Z/Z$ in the order of 3×10^{-14} for nuclear damage with an energy density of 1 J/m^3. (This estimate is based on the assumption of an average neutron energy of 2 MeV [45], since the given neutron flux in Ref. [44] includes only high-energy neutrons >0.1 MeV, and a mean free path of 0.125 m.) For a crystal of 0.3 mm thickness, this corresponds to $\Delta f/f \approx 1\times10^{-10}$ for an energy deposition of 1 J/m^2. In our case, the energy is deposited close to the surface, where the sensitivity to changes of the acoustic impedance is low. For a damage occurring at a depth of 38.8 μm (8 MeV ion energy), the frequency change for a given energy deposition per area is lower by a factor of 0.31 compared with homogeneous deposition, see Appendix B. In addition, the sensitive area of the crystal is larger than the beam, which further reduces the sensitivity by a factor of ≈0.2, yielding an expected $\Delta f/f$ in the order of 6.2×10^{-12} for a nuclear damage of 1 J/m^2 in the beam area (1 mm diameter).

In our experiment with 8 MeV ion irradiation, the nuclear stopping is about 1.9×10^{-3} of the total energy deposited (72 mW for 900 s), or 0.12 J in the beam area. Thus, the observed frequency change of 32 Hz results in an observed $\Delta f/f$ of $\approx3.4\times10^{-11}$ for 1 J/m^2 nuclear energy

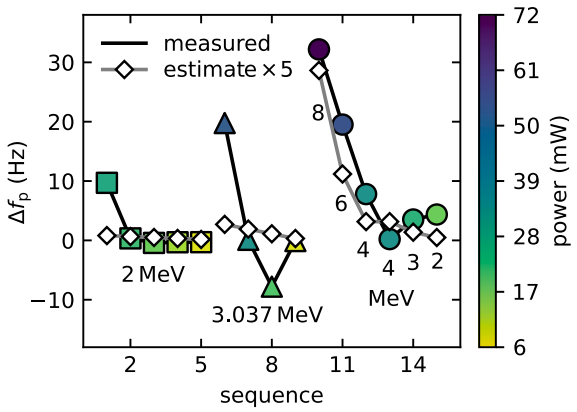

Fig. 12. Persistent frequency changes after a beam-on and a subsequent beam-off-cycle. For the experimental data, the beam power is indicated by the color of the symbols. The data were acquired in three measurement runs, as indicated by different symbol types and connecting lines. The diamonds are rough estimates for the effect of nuclear damage, based on the neutron irradiation experiments by King and Fraser [44], scaled by a factor of 5 (see text).

deposition in the beam area. The discrepancy between the persistent frequency change in our 8 MeV experiment and the estimate of the $\Delta f/f$ sensitivity to nuclear damage based on the neutron experiment in Ref. [44] is a factor of about 5.

Considering the roughness of the approximation, the results appear to be broadly consistent. Generally, the use of neutron irradiation as a proxy for ion irradiation involves approximations. Nevertheless, comparisons based on collisional damage, such as those we have carried out here, are typically considered a reasonable basis for relating ion irradiation damage to neutron damage or vice versa [46,47]. A large uncertainty arises from omitting the effect of the ≈99.8% electronic energy deposition of the ions. This omission is motivated by (i) the fact that most electronic excitations are expected to relax without permanent damage, (ii) the electronic loss is at a shallower depth than the nuclear loss (Fig. 3a); thus, any electronic damage has a weaker effect on the resonance frequency than the nuclear damage deeper inside the crystal, and (iii) as mentioned above, reports in the literature do not report a consistent sign of the frequency change induced by electronic damage. Nevertheless, it is known that electronic excitations induced by electron irradiation can lead to structural damage within SiO_2, e.g., dislocation loops and vitrification [48,49]. Thus, part of the permanent frequency changes might also be caused by damage induced by the electronic stopping. In addition, one has to note that the neutron experiment of Ref. [44] was conducted over a time of 46 days at a crystal temperature of about 150 °C. As it was observed that part of the neutron-induced radiation damage leading to the frequency increase can be annealed out, it is likely that the neutron-induced frequency shift would have been substantially higher at lower temperatures and shorter irradiation time for the same fluence. Also some of our $\Delta f(t)$ data show a slight frequency decrease after the temperature has settled (weakly visible in Fig. 5), indicating that the "persistent" changes might actually decrease over time.

We have calculated the predicted frequency shifts for all data points of Fig. 12, based on the same assumptions as in the previous paragraphs, and using the results of the SRIM calculations for the depth of the Bragg peak and the fraction of nuclear loss for each energy. These estimates, scaled by a factor of 5 for better visualization and to account for the factors discussed in the previous paragraph, are shown as white diamonds in Fig. 12. Based on this plot, we attribute most of the persistent changes at 8 and 6 MeV to damage in the crystal. The Δf_p of the first data points of the first two runs are probably dominated by mass loss due to thermal desorption. This speculation is motivated by the fact that, on the one hand, the effect of damage is expected to be largest for large penetration depths. Thus the effect of damage should be almost negligible for the 2 MeV and 3.037 MeV runs (cf. the white diamonds). On the other hand, thermal desorption is expected to happen only when the crystal reaches a temperature that is substantially higher then the highest temperature it has experienced before. This is the case for the first data point of each run, with beam powers of 30, 51.6 and 72 mW, respectively. The scatter of the experimental data points prevents a more thorough analysis.

The persistent frequency changes discussed here are different from, but superimposed on the transient effects of heating induced by the beam. The frequency change measured at the end of the beam-on phase will include all three contributions discussed here, the temperature change via the frequency-temperature curve (Fig. 2), the thermal stress and the persistent effect of radiation damage and desorption. Thus, for an accurate determination of the crystal temperature, one should subtract the irreversible persistent frequency change from the final frequency of the beam-on phase, which results in a modified $\Delta f^{\mathrm{on}}_{\mathrm{slow}}$ value. Fig. 6b shows that this correction results only in minor changes of $\Delta f^{\mathrm{on}}_{\mathrm{slow}}$ (orange circles vs. orange "×" symbols).

4. Conclusions

We successfully implemented a high-sensitivity QCM in an existing IBA setup at the Tandem Laboratory, Uppsala University. The combination of these techniques is highly advantageous, as the methods complement each other. Our key findings demonstrate that a combination of the QCM and IBA techniques is, in principle, possible. Simultaneous IBA and high-resolution QCM measurements are, however, not possible with the current setup, because thermal effects due to heating by the beam would mask small frequency changes. These thermal effects show two components.

First, heating of the crystal causes "slow" frequency changes caused by the $\Delta f(\vartheta)$ curve of the crystal. Upon switching the beam on or off, the temperature ϑ of the crystal follows an exponential relaxation with a time constant of about two minutes. This time constant is determined by the heat capacity of the quartz crystal and the thermal resistance between the crystal and the holder. While unwanted for operation of the QCM under the ion beam, this frequency change might be also utilized as a thermometer; when measuring the fundamental frequency and the 3rd overtone one can also separate mass and temperature effects [19]. Such a temperature measurement at the sample position could be easier to implement in an IBA setup than a thermocouple [50].

In a future QCM setup optimized for use at an IBA facility, the thermal resistance and thereby the temperature increase could be lowered by using a crystal holder material with better thermal conductivity and increased contact area due to a softer surface (e.g., silver-plated copper). One may also consider using a very soft solder-like metallic contact between the crystal and holder (e.g., with indium), but this bears the risk of diffusion of the solder material onto the crystal electrode surface. Additionally, one must ensure that a solder-like joint does not apply unwanted mechanical stress to the crystal.

The second thermal effect is a fast frequency change when switching the beam on or off. This is mainly due to local stress caused by the inhomogeneous temperature distribution in the crystal. A small contribution to fast frequency changes comes from the fast heating near the impact position of the beam, before the temperature distribution in the crystal equilibrates (thermal diffusivity ≈ 4 mm^2/s). The stress-induced frequency changes strongly depend on the impact position of the beam, which on the one hand demands a stable beam position, on the other hand it provides the opportunity to minimize the problem by selecting a beam position where the fast frequency changes vanish.

Both thermal effects are reversible, i.e. a frequency change of the same magnitude, but in the opposite direction is observed after switching the beam off. We have also observed a persistent frequency increase of up to ≈30 Hz after irradiation by 8 MeV He for 900 s (beam power

72 mW). We attribute most of this frequency change to radiation damage; but also temperature-induced desorption from the electrodes may play a role. Since the sensitivity of the frequency on the damage-induced change of the acoustic impedance approximately scales with the square of the depth of the damaged zone, the influence of radiation damage can be kept low by avoiding high beam energies that would lead to a large penetration depth of the ions.

In conclusion, our study indicates that the combination of QCM and IBA is feasible, but the resolution of small mass changes is limited by beam-induced frequency changes. Our detailed analysis of these effects paves the way to minimizing these unwanted frequency changes. For analyzing small mass changes, it is essential to await thermal equilibration before recording QCM data. The combination of IBA and QCM can then open up new possibilities for future erosion studies as well as elemental analysis and depth profiling measurements.

CRediT authorship contribution statement

Martina Fellinger: Writing – original draft, Visualization, Validation, Investigation, Formal analysis, Data curation, Conceptualization. **Eduardo Pitthan:** Writing – review & editing, Validation, Supervision, Project administration, Methodology, Investigation, Funding acquisition, Data curation, Conceptualization. **Christian Cupak:** Writing – review & editing, Supervision, Methodology, Investigation, Conceptualization. **Friedrich Aumayr:** Writing – review & editing, Supervision, Resources, Funding acquisition, Conceptualization. **Daniel Primetzhofer:** Writing – review & editing, Validation, Supervision, Resources, Funding acquisition, Conceptualization. **Michael Schmid:** Writing – original draft, Visualization, Validation, Supervision, Software, Investigation, Formal analysis, Data curation, Conceptualization.

Declaration of competing interest

The authors declare that they have no known competing financial interests or personal relationships that could have appeared to influence the work reported in this paper.

Acknowledgments

This work has been carried out within the framework of the EUROfusion Consortium, funded by the European Union via the Euratom Research and Training Programme (Grant Agreement No 101052200 — EUROfusion). Views and opinions expressed are however those of the author(s) only and do not necessarily reflect those of the European Union or the European Commission. Neither the European Union nor the European Commission can be held responsible for them. In addition to the EUROfusion program, financial support has also been provided by the Commission for the Coordination of Fusion Research in Austria (KKKÖ) at the Austrian Academy of Sciences (ÖAW). Support of the operation of the tandem accelerator at Uppsala University, Sweden by VR-RFI (contract #2019-00191) is gratefully acknowledged. The authors also acknowledge TU Wien Bibliothek for financial support through its Open Access Funding Programme. The authors would furthermore like to thank Anna Niggas for the fruitful discussions on fundamental physics and Johannes Brötzner and Benjamin Burazor Domazet for the technical exchange on simulation artifacts.

Appendix A. RBS analysis of the electrodes

The IBA setup was used to investigate the elemental composition of the target. An RBS detector, placed at an exit angle of 10 degrees with respect to the surface normal detected the backscattered He particles as a function of their energy. Fig. A.13 shows the measured spectrum for an incident He^+ beam under normal incidence with 2 MeV kinetic energy and a current of 9 nA. The results of a simulation by the SIMNRA [51] software are also included in Fig. A.13. In the simulation, the electrode thickness was adjusted to fit the experimental spectrum by tuning the input layer structure. The best-fit layer structure is sketched in the inset of Fig. A.13. According to this measurement, the target consisted of a SiO_2 bulk, a Cr interlayer of around 0.7 nm and an Au top layer of 76.3 nm in thickness. This layer structure was furthermore used as input for the simulation of the projectile propagation utilizing SRIM, discussed in Section 2.3.

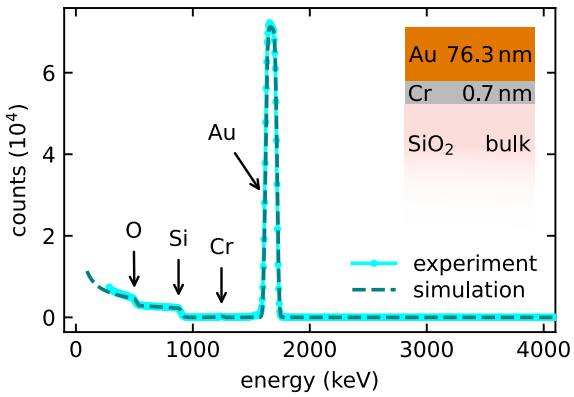

Fig. A.13. RBS spectrum of the QCM sample using 2 MeV He^+ ions for the probing beam. The simulation (dashed line) was performed using SIMNRA [51]. The target input for the simulation consisted of a Au top layer with a thickness corresponding to 450×10^{15} at/cm^2 on a Cr buffer layer (6×10^{15} at/cm^2) on bulk SiO_2, as visualized in the inset.

Appendix B. Resonance frequency of a crystal with a modified inner layer

The influence of the modification of a subsurface layer by nuclear radiation damage (which strongly peaks at a depth close to the penetration depth of the ions, Fig. 3) requires analysis of a three-layer model, different from the usual two-layer model [52,53] used for thick layers of material deposited on a QCM. This analysis can be accomplished with a transfer matrix method [54,55], which we simplify by assuming only one displacement direction and neglecting the influence of piezoelectric stiffening of the elastic constants (or, equivalently, analyzing the parallel resonance, where the crystal impedance would be infinite in the absence of losses; this frequency is unaffected by the piezoelectric constants). For each layer (with a thickness d, sound velocity v and acoustic impedance Z), the transfer matrix for a vector containing the displacement velocity $\dot{u}$ and stress σ is given by[1]

$$\mathbf{M} = \begin{pmatrix} M^{\dot{u}\dot{u}} & M^{\dot{u}\sigma} \\ M^{\sigma\dot{u}} & M^{\sigma\sigma} \end{pmatrix} = \begin{pmatrix} \cos\frac{\omega d}{v} & \frac{1}{Z}\sin\frac{\omega d}{v} \\ -Z\sin\frac{\omega d}{v} & \cos\frac{\omega d}{v} \end{pmatrix} \tag{B.1}$$

Note that the terms d/v in the arguments of the sin and cos functions can be also written as m_A/Z.

For three layers, the overall transfer matrix $\mathbf{M}$ is given by the product of the three transfer matrices $\mathbf{M}_i$ of the individual layers. Since the surfaces are stress-free, $M^{\sigma\dot{u}}$ of this overall matrix $\mathbf{M}$ must vanish. This leads to

$$Z_1 \tan\frac{\omega d_1}{v_1} + Z_2 \tan\frac{\omega d_2}{v_2} + Z_3 \tan\frac{\omega d_3}{v_3} - \frac{Z_1 Z_3}{Z_2} \tan\frac{\omega d_1}{v_1} \tan\frac{\omega d_2}{v_2} \tan\frac{\omega d_3}{v_3} = 0\,, \tag{B.2}$$

which determines the (angular) resonance frequency ω. If layers 1 and 3 are unperturbed quartz with an acoustic impedance Z, in the limit

[1] In contrast to Ref. [54], we use $\dot{u}$ instead of the displacement u, which simplifies the equations. For the stress, we write σ instead of T, for consistency with Appendix D.

of a thin subsurface layer 2 with a perturbed impedance Z_2, implicit differentiation yields the influence of Z_2 on the resonance frequency

$$\frac{\mathrm{d}f}{\mathrm{d}Z_2} = \frac{2f}{Z}\frac{d_2}{d}\sin^2\frac{d_1\pi}{d}\ , \tag{B.3}$$

where d is the overall thickness (sum of the three d_i). As we have expressed the perturbation via the acoustic impedance Z_2 of the subsurface layer and kept the mass per area constant, similar to the right-hand term of Eq. (1), Eq. (B.3) is valid not only for a change in elastic constants of the subsurface layer but also if its thickness d_2 expands or contracts.

As mentioned in the introduction, for changes in the elastic constants in a subsurface layer, the influence of the perturbation scales with the square of the vibrational stress or strain, which have a node at the surface. Thus, for a shallow perturbed layer, its influence scales with the square of its depth d_1 below the surface. (d_1 is the thickness of the layer above the perturbed layer 2, but it may also be taken as the thickness of the layer below; the result is the same due to the periodicity of the sin function.) The same perturbation argument could also be used to derive Eq. (B.3) in a simple way: The stress or strain as a function of the distance d_1 from the surface is proportional to $\sin\frac{d_1\pi}{d}$; thus, the influence of the perturbation scales with the $\sin^2$ function of Eq. (B.3). When perturbing the whole thickness of the quartz crystal, we can either calculate the frequency change by integrating Eq. (B.3) over all depths d_1 or from Eq. (1); both must result in the same frequency change. This equality determines the prefactor of the $\sin^2$ function in Eq. (B.3). For the case of a radiation dose changing the acoustic impedance of a crystal, under the assumption that the change ΔZ is proportional to the dose per volume, Eq. (B.3) implies that the frequency change per dose deposited at a depth d_1 is $2\sin^2\frac{d_1\pi}{d}$ times the frequency change caused by the same dose equally distributed in the whole volume of the crystal.

Appendix C. Thermal conductivity and elasticity tensors of a plate consisting of an anisotropic material

As mentioned in Section 2.4, the thermal conductivity λ and elasticity c tensors required in a 2D calculation for a thin plate cannot be obtained by simply skipping the out-of-plane components of the 3D tensors. For thermal conductivity, we have (using Einstein summation convention)

$$q_i = \lambda_{ij}\partial_j T\ , \tag{C.1}$$

where q is the heat flux and $\partial_j T$ the jth component of the temperature gradient. In a 2D calculation, we require that the heat flow is parallel to the surface ($q_\perp = 0$). For an anisotropic material, however, the temperature gradient can have a nonzero component in the normal direction. Therefore, one cannot simply skip the out-of-plane components of λ. Using the inverse matrix λ^{-1}, we can write

$$\partial_i T = \lambda^{-1}_{ij} q_j\ . \tag{C.2}$$

Since we are not interested in the temperature gradient in the normal direction, we can skip the out-of-plane components of λ^{-1}. This reduces λ^{-1} from a (3×3) to a (2×2) matrix. Taking the inverse of this (2×2) matrix yields the thermal conductivity tensor required for the 2D calculation. In the conventional coordinate system of an SC-cut quartz crystal, the normal direction is y. Thus, the "y" column and "y" row of the λ^{-1} matrix can be removed.

Similarly, the equation for elastic deformation without thermal expansion is

$$\sigma_{ij} = c_{ijkl}\epsilon_{kl}\ , \tag{C.3}$$

with the stress σ and strain ϵ. If the y direction (index 2) is normal to the surface, the boundary conditions at the surface are $\sigma_{2j} = 0$ [31]. Again, we have to invert the matrix, which leads to the compliance tensor s. (In practice, the inversion is easily done as a simple matrix inversion in Voigt notation, which has only two, not four indices for c and s.) The equation then reads

$$\epsilon_{ij} = s_{ijkl}\sigma_{kl}\ . \tag{C.4}$$

For static deformations of a thin plate, in the absence of bending, the stress does not depend on the normal direction y. Thus, the boundary conditions imply that σ_{kl} is zero if $k = 2$ or $l = 2$. We are only interested in strain components related to in-plane displacements, thus any components on the left side of Eq. (C.4) having at least one index 2 (y direction) are irrelevant. This means that we can skip all s components with any index 2, converting s from a tensor in 3D to 2D. The elasticity tensor c required for the 2D calculation is then obtained as the inverse of this 2D version of s. (Again, the inverse can be easily calculated as a matrix inversion in Voigt notation.)

Appendix D. Elasticity with thermal expansion in FreeFEM++

Since the FreeFEM++ documentation does not cover the case of anisotropic elasticity coupled with thermal expansion, we provide the relevant equations here. We start from the equation [56]

$$\partial_j\sigma_{ij} = \partial_j c_{ijkl}(\epsilon_{kl} - \alpha_{kl}\Delta T) = 0, \tag{D.1}$$

where α is the tensor of thermal expansion coefficients, and $\Delta T = T - T_0$, with T_0 being the reference temperature for the thermal expansion. The implementation inFreeFEM++ is based on a variational principle (the weak formulation) [30] for the displacement field u, written here for Dirichlet boundary conditions:

$$\int \left(\partial_j c_{ijkl}\epsilon_{kl}(u)\right) v_i\,\mathrm{d}^2r - \int (\partial_j c_{ijkl}\alpha_{kl}\Delta T)v_i\,\mathrm{d}^2r = 0\ , \tag{D.2}$$

which should be valid for all test functions v fulfilling the boundary conditions. Integration by parts yields the form required by FreeFEM++:

$$\begin{aligned} &-\int c_{ijkl}\epsilon_{kl}(u)\partial_j v_i\,\mathrm{d}^2r + \int c_{ijkl}\alpha_{kl}\Delta T\partial_j v_i\,\mathrm{d}^2r \\ &\quad + \left[c_{ijkl}\epsilon_{kl}(u)n_j v_i\right]_\Gamma - \left[c_{ijkl}\alpha_{kl}\Delta T n_j v_i\right]_\Gamma = 0, \end{aligned} \tag{D.3}$$

where Γ is the boundary. The terms loosely written in square brackets as "$[\dots]_\Gamma$" (to demonstrate the relation to the more familiar integration by parts in one dimension) are one-dimensional integrals along the boundary, with n being the normal vector.

Since we calculate the stress-induced frequency change only for the steady state, our calculation does not include the temperature increase due to adiabatic compression of the crystal occurring during transients [57]. For quartz, this effect is negligible; it is related to the difference between the isothermal and adiabatic elastic constants, which is less than 2% for quartz at room temperature [58]. When calculating the temperature increase, we also neglect the conversion of a fraction of the deposited energy into elastic energy: Even at the highest power considered here, 70 mW, the elastic energy is only 1.5 mJ in steady-state conditions. For comparison, with Dirichlet boundary conditions (constant temperature at the border), the thermal energy in the crystal (related to its heat capacity) is 223 mJ. When taking the thermal resistance at the boundary into account, the crystal reaches a higher temperature and the thermal energy reaches almost 10 J. Thus, only a tiny fraction of the energy deposited by the ion beam gets converted into elastic energy. Since the elastic energy scales with the square of the stress, this fraction is even lower if the power of the incident beam is less.

For the conversion of stress to a frequency shift, we use a fit to the angle-dependent force-frequency coefficient of an SC quartz disk given in Ref. [59], resulting in

$$\begin{aligned} \Delta f/f\ =\ &-6.449\times10^{-7}\sigma_{xx} - 1.734\times10^{-5}\sigma_{xz} \\ &+6.898\times10^{-7}\sigma_{zz} \end{aligned} \tag{D.4}$$

where the stresses σ are in N/mm^2. The local stresses (or equivalently, their local contribution to $\Delta f/f$) are weighted with the Gaussian sensitivity curve of the QCM crystal (Fig. 1).

Appendix E. Supplementary material

Computer codes used for this article can be found online as supplementary material at https://doi.org/10.1016/j.apsusc.2026.167107.

Data availability

Data will be made available on request.

References

[1] G. Sauerbrey, Verwendung von Schwingquarzen zur Wägung dünner Schichten und zur Mikrowägung, Z. Phys. 155 (1959) 206–222, http://dx.doi.org/10.1007/BF01337937.

[2] E. Benes, M. Schmid, G. Thorn, Progress in monitoring thin film thickness by use of quartz crystals, Thin Solid Films 174 (1989) 307–314, http://dx.doi.org/10.1016/0040-6090(89)90907-3.

[3] E. Benes, M. Gröschl, W. Burger, M. Schmid, Sensors based on piezoelectric resonators, Sensors Actuators A 1 (48) (1995) 1–21, http://dx.doi.org/10.1016/0924-4247(95)00846-2.

[4] D.S. Katzer, N. Nepal, D.J. Meyer, B.P. Downey, V.D. Wheeler, D.F. Storm, M.T. Hardy, Epitaxial metallic β-Nb_2N films grown by MBE on hexagonal SiC substrates, Appl. Phys. Express 8 (8) (2015) 085501, http://dx.doi.org/10.7567/APEX.8.085501.

[5] G. Franceschi, M. Schmid, U. Diebold, M. Riva, Movable holder for a quartz crystal microbalance for exact growth rates in pulsed laser deposition, Rev. Sci. Instrum. 91 (6) (2020) 065003, http://dx.doi.org/10.1063/5.0007643.

[6] B.M. Berger, P.S. Szabo, R. Stadlmayr, F. Aumayr, Sputtering measurements using a quartz crystal microbalance as a catcher, Nucl. Instrum. Methods Phys. Res. B 406 (2017) 533–537, http://dx.doi.org/10.1016/j.nimb.2016.11.039.

[7] S. Brezinsek, A. Kirschner, M. Mayer, A. Baron-Wiechec, I. Borodkina, D. Borodin, I. Coffey, J. Coenen, N. Den Harder, A. Eksaeva, et al., Erosion, screening, and migration of tungsten in the JET divertor, Nucl. Fusion 59 (9) (2019) 096035, http://dx.doi.org/10.1088/1741-4326/ab2aef.

[8] S. Brezinsek, J. Coenen, T. Schwarz-Selinger, K. Schmid, A. Kirschner, A. Hakola, F. Tabares, H. Van Der Meiden, M.-L. Mayoral, M. Reinhart, et al., Plasma–wall interaction studies within the EUROfusion consortium: Progress on plasma-facing components development and qualification, Nucl. Fusion 57 (11) (2017) 116041, http://dx.doi.org/10.1088/1741-4326/aa796e.

[9] J. Linke, J. Du, T. Loewenhoff, G. Pintsuk, B. Spilker, I. Steudel, M. Wirtz, Challenges for plasma-facing components in nuclear fusion, Matter Radiat. Extrem. 4 (5) (2019) 056201, http://dx.doi.org/10.1063/1.5090100.

[10] G. Hayderer, M. Schmid, P. Varga, H. Winter, F. Aumayr, A highly sensitive quartz-crystal microbalance for sputtering investigations in slow ion–surface collisions, Rev. Sci. Instrum. 70 (9) (1999) 3696–3700, http://dx.doi.org/10.1063/1.1149979.

[11] C. Cupak, P. Szabo, H. Biber, R. Stadlmayr, C. Grave, M. Fellinger, J. Brötzner, R. Wilhelm, W. Möller, A. Mutzke, et al., Sputter yields of rough surfaces: Importance of the mean surface inclination angle from nano- to microscopic rough regimes, Appl. Surf. Sci. 570 (2021) 151204, http://dx.doi.org/10.1016/j.apsusc.2021.151204.

[12] A. Lopez-Cazalilla, C. Cupak, M. Fellinger, F. Granberg, P.S. Szabo, A. Mutzke, K. Nordlund, F. Aumayr, R. González-Arrabal, Comparative study regarding the sputtering yield of nanocolumnar tungsten surfaces under Ar^+ irradiation, Phys. Rev. Mater. 6 (7) (2022) 075402, http://dx.doi.org/10.1103/PhysRevMaterials.6.075402.

[13] J. Brötzner, C. Cupak, M. Fellinger, H. Biber, A. Lopez-Cazalilla, F. Granberg, F. Kporha, A. Mutzke, R. González-Arrabal, F. Aumayr, Sputtering yield reduction for nano-columnar W surfaces under D ion irradiation, Nucl. Mater. Energy 37 (2023) 101507, http://dx.doi.org/10.1016/j.nme.2023.101507.

[14] A. Golczewski, A. Kuzucan, K. Schmid, J. Roth, M. Schmid, F. Aumayr, Ion-induced erosion of tungsten surfaces studied by a sensitive quartz-crystal-microbalance technique, J. Nucl. Mater. 390–391 (2009) 1102–1105, http://dx.doi.org/10.1016/j.jnucmat.2009.01.279.

[15] C.M. Pieters, S.K. Noble, Space weathering on airless bodies, J. Geophys. Res.: Planets 121 (10) (2016) 1865–1884, http://dx.doi.org/10.1002/2016JE005128.

[16] A. Galli, A. Vorburger, P. Wurz, M. Tulej, Sputtering of water ice films: A re-assessment with singly and doubly charged oxygen and argon ions, molecular oxygen, and electrons, Icarus 291 (2017) 36–45, http://dx.doi.org/10.1016/j.icarus.2017.03.018.

[17] P.S. Szabo, Experimental And Simulated Sputtering of Gold, Iron and Wollastonite with a Catcher-QCM Setup (Master's thesis), TU Wien, 2017, http://dx.doi.org/10.34726/hss.2017.37338.

[18] J. Brötzner, H. Biber, P.S. Szabo, N. Jäggi, L. Fuchs, A. Nenning, M. Fellinger, G. Nagy, E. Pitthan, D. Primetzhofer, et al., Sputter yields of the lunar surface: Experimental validation and numerical modelling of solar wind sputtering of Apollo 16 soils, Commun. Earth Env. 6 (1) (2025) 560, http://dx.doi.org/10.1038/s43247-025-02546-0.

[19] R. Stadlmayr, P.S. Szabo, H. Biber, H.R. Koslowski, E. Kadletz, C. Cupak, R.A. Wilhelm, M. Schmid, C. Linsmeier, F. Aumayr, A high temperature dual-mode quartz crystal microbalance technique for erosion and thermal desorption spectroscopy measurements, Rev. Sci. Instrum. 91 (12) (2020) 125104, http://dx.doi.org/10.1063/5.0012028.

[20] J. Perrière, Rutherford backscattering spectrometry, Vacuum 37 (5–6) (1987) 429–432, http://dx.doi.org/10.1016/0042-207X(87)90327-7.

[21] W.M. Arnold Bik, F.H.P.M. Habraken, Elastic recoil detection, Rep. Progr. Phys. 56 (7) (1993) 859, http://dx.doi.org/10.1088/0034-4885/56/7/002.

[22] P. Ström, D. Primetzhofer, Ion beam tools for nondestructive in-situ and in-operando composition analysis and modification of materials at the Tandem Laboratory in Uppsala, J. Instrum. 17 (2022) P04011, http://dx.doi.org/10.1088/1748-0221/17/04/P04011.

[23] E. Pitthan, C. Cupak, M. Fellinger, M. Moro, S. Kioumourtzoglou, D. Moldarev, M. Wolff, F. Aumayr, D. Primetzhofer, In-situ, real-time investigation of the formation of oxygen-containing rare-earth hydrides by combining a quartz crystal microbalance and ion beam analysis, Materialia 27 (2023) 101675, http://dx.doi.org/10.1016/j.mtla.2023.101675.

[24] E. EerNisse, Quartz resonator frequency shifts arising from electrode stress, in: 29th Annual Symposium on Frequency Control, IEEE, 1975, pp. 1–4, http://dx.doi.org/10.1109/FREQ.1975.200056.

[25] D.S. Stevens, H.F. Tiersten, An analysis of doubly rotated quartz resonators utilizing essentially thickness modes with transverse variation, J. Acoust. Soc. Am. 79 (6) (1986) 1811–1826, http://dx.doi.org/10.1121/1.393190.

[26] T. Shiono, Y. Osada, Y. Nakagawa, Frequency change of quartz crystal resonator caused during ion beam etching, Japan. J. Appl. Phys. 46 (2007) 4647–4651, http://dx.doi.org/10.1143/JJAP.46.4647.

[27] J. Zelenka, Piezoelectric Resonators and Their Applications, Studies in electrical and electronic engineering, Vol. 24, Elsevier, Amsterdam, 1986.

[28] K. Kantre, M. Moro, D. Moldarev, D. Johansson, D. Wessman, M. Wolff, D. Primetzhofer, SIGMA: A Set-up for In-situ Growth, Material modification and Analysis by ion beams, Nucl. Instrum. Methods Phys. Res. B 463 (2020) 96–100, http://dx.doi.org/10.1016/j.nimb.2019.11.007.

[29] J.F. Ziegler, M. Ziegler, J. Biersack, SRIM – The stopping and range of ions in matter (2010), Nucl. Instrum. Methods Phys. Res. B 268 (11–12) (2010) 1818–1823, http://dx.doi.org/10.1016/j.nimb.2010.02.091.

[30] F. Hecht, New development in freefem++, J. Numer. Math. 20 (3–4) (2012) 251–266, http://dx.doi.org/10.1515/jnum-2012-0013.

[31] IEEE Standard on Piezoelectricity, IEEE, New York, 1988, http://dx.doi.org/10.1109/IEEESTD.1988.79638.

[32] M.W. Chase, NIST-JANAF thermochemical tables, J. Phys. Chem. Ref. Data Monograph 9 (1998) 1–1951.

[33] J.W. Vandersande, C. Wood, The thermal conductivity of insulators and semiconductors, Contemp. Phys. 27 (2) (1986) 117–144, http://dx.doi.org/10.1080/00107518608211003.

[34] M.J. Assael, K. Gialou, Measurement of the thermal conductivity of stainless steel AISI 304L up to 550 K, Int. J. Thermophys. 24 (2003) 1145–1153, http://dx.doi.org/10.1023/A:1025069405106.

[35] L.N. Aksyutov, Normal spectral emissivity of gold, platinum, and tungsten, J. Eng. Phys. 27 (2) (1974) 913–917, http://dx.doi.org/10.1007/BF00861593.

[36] P. Lee, M. Tang, Thickness vibrations of doubly rotated crystal plates under initial deformations, IEEE Trans. Ultrason. Ferroelectr. Freq. Control 34 (6) (1987) 659–666, http://dx.doi.org/10.1109/T-UFFC.1987.26999.

[37] L. Clayton, E. Eernisse, Frequency shift calculations for quartz resonators, in: Proceedings of the 45th Annual Symposium on Frequency Control, IEEE, 1991, pp. 309–320, http://dx.doi.org/10.1109/FREQ.1991.145916.

[38] H. Minagawa, H. Tsuchida, Possibility of the existence of a topological defect in dynamic deformation of the free-standing ultrathin silicon wafer during MeV ion irradiation, J. Appl. Phys. 131 (8) (2022) 085701, http://dx.doi.org/10.1063/5.0077180.

[39] T.M. Flanagan, R.E. Leadon, D.L. Shannon, Evaluation of mechanisms for low-dose frequency shifts in crystal oscillators, IEEE Trans. Nucl. Sci. 33 (6) (1986) 1447–1453, http://dx.doi.org/10.1109/TNS.1986.4334621.

[40] R. Filler, J. Vig, Fundamental mode SC-cut resonators, in: 34th Annual Symposium on Frequency Control, IEEE, 1980, pp. 187–193, http://dx.doi.org/10.1109/FREQ.1980.200401.

[41] A. von Hippel, C. Breakdown. Electric breakdown of solid dielectrics, Trans. Faraday Soc. 42 (1946) 78–87, http://dx.doi.org/10.1039/TF946420A078.

[42] J. Norton, BVA-type quartz oscillator for spacecraft, in: Proceedings of the 45th Annual Symposium on Frequency Control, IEEE, 1991, pp. 426–430, http://dx.doi.org/10.1109/FREQ.1991.145931.

[43] J.R. Norton, J.M. Cloeren, J.J. Suter, Results from Gamma ray and proton beam radiation testing of quartz resonators, IEEE Trans. Nucl. Sci. 31 (6) (1984) 1230–1235, http://dx.doi.org/10.1109/TNS.1984.4333488.

[44] J. King, D. Fraser, Effects of reactor irradiation on thickness shear crystal resonators, in: 16th Annual Symposium on Frequency Control, IEEE, 1962, pp. 7–32, http://dx.doi.org/10.1109/FREQ.1962.199496.

[45] B. Watt, Energy spectrum of neutrons from thermal fission of U^{235}, Phys. Rev. 87 (6) (1952) 1037, http://dx.doi.org/10.1103/PhysRev.87.1037.

[46] S.J. Zinkle, L.L. Snead, Opportunities and limitations for ion beams in radiation effects studies: Bridging critical gaps between charged particle and neutron irradiations, Scr. Mater. 143 (2018) 154–160, http://dx.doi.org/10.1016/j.scriptamat.2017.06.041.

[47] W.A. Hanson, M.K. Patel, M.L. Crespillo, F. Zhang, S.J. Zinkle, Y. Zhang, W.J. Weber, Ionizing vs collisional radiation damage in materials: Separated, competing, and synergistic effects in Ti_3SiC_2, Acta Mater. 173 (2019) 195–205, http://dx.doi.org/10.1016/j.actamat.2019.05.015.

[48] G. Das, T.E. Mitchell, Electron irradiation damage in quartz, Radiat. Eff. 23 (1) (1974) 49–52, http://dx.doi.org/10.1080/00337577408232044.

[49] C.B. Carter, D.L. Kohlstedt, Electron irradiation damage in natural quartz grains, Phys. Chem. Miner. 7 (3) (1981) 110–116, http://dx.doi.org/10.1007/BF00308226.

[50] M.L. Crespillo, J.T. Graham, Y. Zhang, W.J. Weber, Temperature measurements during high flux ion beam irradiations, Rev. Sci. Instrum. 87 (2) (2016) 024902, http://dx.doi.org/10.1063/1.4941720.

[51] M. Mayer, SIMNRA, a simulation program for the analysis of NRA, RBS and ERDA, AIP Conf. Proc. 475 (1999) 541–544, http://dx.doi.org/10.1063/1.59188.

[52] J.G. Miller, D.I. Bolef, Acoustic wave analysis of the operation of quartz-crystal film-thickness monitors, J. Appl. Phys. 39 (12) (1968) 5815–5816, http://dx.doi.org/10.1063/1.1656066.

[53] C.-S. Lu, O. Lewis, Investigation of film-thickness determination by oscillating quartz resonators with large mass load, J. Appl. Phys. 43 (11) (1972) 4385–4390, http://dx.doi.org/10.1063/1.1660931.

[54] H. Nowotny, E. Benes, General one-dimensional treatment of the layered piezoelectric resonator with two electrodes, J. Acoust. Soc. Am. 82 (2) (1987) 513–521, http://dx.doi.org/10.1121/1.395453.

[55] H. Nowotny, E. Benes, M. Schmid, Layered piezoelectric resonators with an arbitrary number of electrodes (general one-dimensional treatment), J. Acoust. Soc. Am. 90 (3) (1991) 1238–1245, http://dx.doi.org/10.1121/1.401915.

[56] J.D. Renton, Applied Elasticity: Matrix and Tensor Analysis of Elastic Continua, second ed., Horwood Publishing, Chichester, 2005.

[57] R. Holland, Nonuniformly heated anisotropic plates: I. Mechanical distortion and relaxation, IEEE Trans. Son. Ultrason. 21 (3) (1974) 171–177, http://dx.doi.org/10.1109/T-SU.1974.29811.

[58] R. Bechmann, Elastic and piezoelectric constants of alpha-quartz, Phys. Rev. 110 (5) (1958) 1060–1061, http://dx.doi.org/10.1103/PhysRev.110.1060.

[59] L.D. Clayton, E.P. Eernisse, Quartz resonator frequency shifts computed using the finite element method, Internat. J. Numer. Methods Engrg. 36 (3) (1993) 385–401, http://dx.doi.org/10.1002/nme.1620360303.